ARMY RESEARCH LABORATORY

Observation of Real Time Magnetization Inversion-recovery Using the SPAM Geometry and the CERMIT Protocol

by Dimitri A. Alexson and Doran D. Smith

ARL-TR-5742 **September 2011**

NOTICES

Disclaimers

The findings in this report are not to be construed as an official Department of the Army position unless so designated by other authorized documents.

Citation of manufacturer's or trade names does not constitute an official endorsement or approval of the use thereof.

Destroy this report when it is no longer needed. Do not return it to the originator.

Army Research Laboratory
Adelphi, MD 20783-1197

ARL-TR-5742 **September 2011**

Observation of Real Time Magnetization Inversion-recovery Using the SPAM Geometry and the CERMIT Protocol

Dimitri A. Alexson and Doran D. Smith
Sensors and Electron Devices Directorate, ARL

REPORT DOCUMENTATION PAGE

Form Approved
OMB No. 0704-0188

1. REPORT DATE *(DD-MM-YYYY)*	2. REPORT TYPE	3. DATES COVERED (From - To)
September 2011		June 2011

4. TITLE AND SUBTITLE
Observation of Real Time Magnetization Inversion-recovery Using the SPAM Geometry and the CERMIT Protocol

5a. CONTRACT NUMBER

5b. GRANT NUMBER

5c. PROGRAM ELEMENT NUMBER

6. AUTHOR(S)
Dimitri A. Alexson and Doran D. Smith

5d. PROJECT NUMBER

5e. TASK NUMBER

5f. WORK UNIT NUMBER

7. PERFORMING ORGANIZATION NAME(S) AND ADDRESS(ES)
U.S. Army Research Laboratory
ATTN: RDRL-SEE-O
2800 Powder Mill Road
Adelphi, MD 20783-1197

8. PERFORMING ORGANIZATION REPORT NUMBER
ARL-TR-5742

9. SPONSORING/MONITORING AGENCY NAME(S) AND ADDRESS(ES)

10. SPONSOR/MONITOR'S ACRONYM(S)

11. SPONSOR/MONITOR'S REPORT NUMBER(S)

12. DISTRIBUTION/AVAILABILITY STATEMENT
Approved for public release; distribution unlimited.

13. SUPPLEMENTARY NOTES

14. ABSTRACT
We mechanically measure in real time the recovery of nuclear magnetization in an inversion-recovery experiment using a force gradient protocol by monitoring the frequency of a driven cantilever. The Ga69 polarization is initially inverted with a wide adiabatic rapid passage sweep lasting 20 ms. After inverting the polarization, we observe in real time the initial <50 mHz transient decay back to the base line as the polarization realigns along the Zeeman axis with a T_1 of approximately 20 min for T = 4.8 K. The magnetization is shown to be inversely linear with temperature. The RF is on only during the adiabatic rapid passage sweep.

15. SUBJECT TERMS

16. SECURITY CLASSIFICATION OF:			17. LIMITATION OF ABSTRACT	18. NUMBER OF PAGES	19a. NAME OF RESPONSIBLE PERSON
a. REPORT	b. ABSTRACT	c. THIS PAGE	UU	24	Dimitri A. Alexson
Unclassified	Unclassified	Unclassified			19b. TELEPHONE NUMBER (*Include area code*) (301) 394-2523

Standard Form 298 (Rev. 8/98)
Prescribed by ANSI Std. Z39.18

Contents

List of Figures

List of Tables

INTENTIONALLY LEFT BLANK.

1. Introduction

A common technique in magnetic resonance is the measurement of T_1 with an inversion recovery experiment. Knowledge of T_1 finds use in many areas, i.e., superconductors (*1*), semiconductors (*2*), and organic materials (*3*). Modern electrically detected NMR instruments are only sensitive to the transverse magnetization. They perform this measurement while measuring the precession of magnetization in the XY plane. In solids, this is typically a very short time, the order of 100 μs. An inversion recovery experiment is performed by inverting the magnetization, waiting some fraction of the T_1 time, laying the remaining polarization in the XY plane and measuring its magnitude by measuring the size of the free induction decay (FID). One must then wait for the order of T_1 for the magnetization to recover before performing the experiment over again. To obtain N points on the T_1 curve takes time equal to the order of $N*T_1$. We demonstrate a technique suggested by John Marohn (*4*) where the entire saturation recovery curve is obtained in one experiment lasting time equal to the order of T_1. Using a MEMS cantilever in a mechanically detected NMR experiment, we measure the entire inversion recovery curve after a single adiabatic rapid passage (ARP) sweep through resonance that inverts the initial polarization. The experiments are performed with a magnetic resonance force microscopy (MRFM) (*5*) tool operating in the springiness preservation by aligning magnetization (SPAM) (*6*) geometry using the cantilever enhanced resonance magnetization inversion transients (CERMIT) protocol. The signal is registered as a change in the resonant frequency of a soft ($k \sim 10^{-4}$ N/m) cantilever with a Ni sphere attached to the free end, operating in vacuum, at 5 K, in a 5 T magnetic field using Ga69 in a GaAs crystal.

2. System Description and Methods

The MRFM probe consists of two major subsystems, a probe body and a probe head. The probe body consists of three major parts: (1) a room temperature flange that mates with the top of the experimental Dewar to which all vacuum, electrical and optical connections are made, (2) the probe head body which is a 4 K grease sealed (*11*) vacuum can, and (3) two thin-walled stainless steel tubes that suspend the vacuum can from the room temperature flange. The probe head is contained inside the probe head body.

The MRFM probe head body has a 2.5 in outer diameter and is vertically inserted into the 2.5 in clear bore of a 9 T superconducting magnet. Both the magnet and probe head body are cooled by direct immersion in liquid He. One of the two thin walled stainless steel tubes has a ¼ inch outside diameter, and the other has a ½ inch outside diameter. The ½ inch tube is used to evacuate the probe and both tubes carry electrical wires and optical fibers from the room

temperature side to the cold end of the probe. The RF power is fed to the probe head via silver coated stainless steel coax that is routed outside the tubes and enters the probe head body just above the grease seal. By routing the RF coax through the liquid helium, the heat that conducts down the coax, or is generated by RF dissipation, is dissipated in the liquid helium bath and not conducted into the probe head.

Inside the probe head body the probe head is suspended from the top of the body by three BeCu springs. A Teflon rod with rounded ends is ensheathed by each spring. The Teflon rods act as frictional dampers to vibrations traveling down the springs from the probe body to the probe head (*8*). Measurements of probe head vibrations with and without the Teflon rods confirm that they do damp vibrations (*10*). All wires and optical fibers spanning the probe-body probe-head gap must not conduct too many vibrations into the probe head. This is especially an issue with the RF subsystem, which includes the RF tank circuit and RF coil. The RF dissipates up to 1 W in the probe head and the resulting heat must be conducted out without coupling vibrations into the probe head. To accomplish this we use three Cu foils 6*9's pure, 50 microns thick, 1 cm wide, and 20 cm long. This is a tradeoff because we need enough Cu foil to conduct the heat out, but not so much that vibrations are coupled into the probe head.

The four main elements of the probe head, as shown in figure 1, are a cantilever with a ferromagnetic particle attached to its free end, optical fiber, RF coil, and sample mounted on a sample stage. The optical fiber is used to sense the position of the cantilever. The RF coil is used to generate an RF magnetic field B_1 which excites the nuclei in the sample. The sample stage moves 5 mm in each of three dimensions and is used to position the sample relative to the fixed cantilever. The silicon cantilevers used are typically 450 microns long, 5 microns wide, and 300 nm thick. They have a 30 micron diameter optical reflection pad centered 70 microns from the free end of the cantilever. Attached to the free end of the cantilever and overhanging it is a 6 microns diameter Ni particle. The several Tesla magnetic field used for the experiments fully magnetizes the Ni particle. The cantilever's amplitude is controlled by a piezoelectric stack that vibrates the base of the cantilever in an open loop configuration. The frequency of the cantilever is controlled in a closed loop feedback configuration, which keeps the cantilever oscillating at its natural frequency. This allows the use of the CERMIT protocol, which relates the change in the cantilever's frequency to a change in the magnitude of the net magnetization along the Zeeman axis.

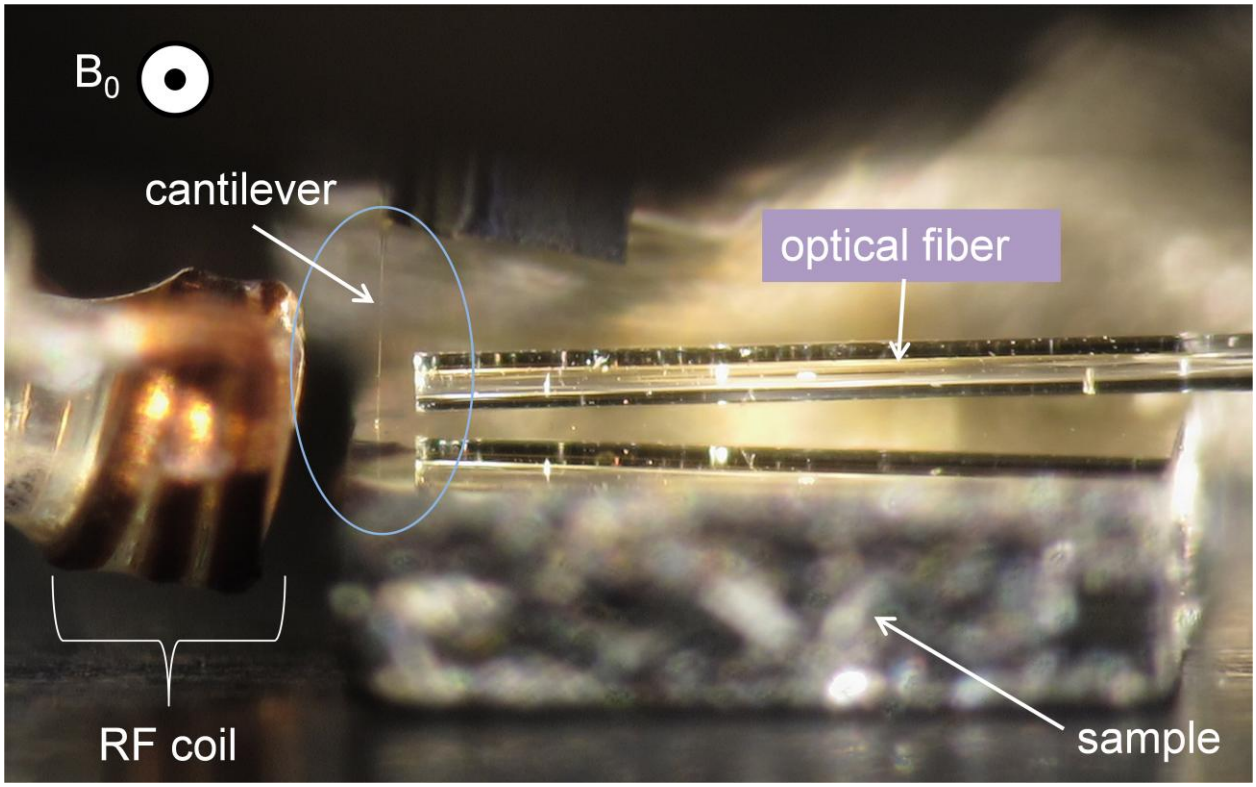

Figure 1. MRFM setup in the SPAM geometry. Shown are the four main elements: the sample, bare optical fiber, cantilever with Ni particle attached to the free end and the RF coil. B_0 is in/out of the page with B_1 and the oscillation of the cantilever in the plane of the page. The optical fiber is standard 9/125 micron fiber. The RF coil consists of 2.5 turns of 100 microns diameter 6*9 Cu wire wound with a 500 microns inner diameter.

The four items that constitute the probe head must be positioned within a few micrometers of each other. The challenging aspect of the design is the items are positioned at room temperature in air, but must remain aligned as the probe head is evacuated and cooled down to 4 K. Small mechanical distances and thermally compensated design principles are used. The mechanical frame of the probe head, meaning those parts of the probe head responsible for maintaining alignment on cool down, are made entirely of type II Ti and are assembled with brass screws. As brass shrinks twice as much as Ti does on being cooled from room temperature to 4 K, the probe parts are compressed together even tighter once cooled. The position of the cantilever is fixed in the probe head. The fiber and RF coil are each independently aligned to the cantilever's position before cool down. The sample stage is approximately aligned before cool down, with final alignment occurring once the probe is cold.

The cantilever oscillation is sensed by an optical interferometer operating at 1300 nm. The two reflective surfaces that form the Fabry-Perot cavity are the optical reflection pad on the cantilever and the 0° angle cleaved face of a single mode optical fiber. The end of the optical fiber is positioned approximately 100 microns from the cantilever's reflection pad. Four percent of the light coming down the fiber is reflected at the glass-air interface back up the fiber. The

remaining laser light exits the fiber as a Gaussian beam. A fraction of the laser light strikes the cantilever's reflection pad and is reflected back towards the fiber. This results in two light beams traveling back up the fiber. Since the fiber-cantilever gap is smaller than the light's coherence length, the two beams traveling up the fiber are phase coherent. These two beams are picked off the fiber with a 90:10 directional coupler and detected with a square law detector. The interference of the two beams with each other forms an interferometer sensitive to picometer displacements of the cantilever. The total interferometer package, optics plus electronics, has a 1 pm per root Hz noise floor.

The RF coil is formed from 2.5 turns of 100 micron diameter 6*9 Cu wire wound with a 500 micron inner diameter. Since B_1 falls off with the distance r, for $r \gg a$, from the face of the coil as (a^2/r^3) where a is the radius the RF coil, the coil is positioned within 150 micrometers of the cantilever and the edge of the sample. In this region, where $r \sim a$, the drop off in B_1 is linear with r, so the exact positioning from the sample is more forgiving. The RF circuit produces 1.06 mT of B_1 for 1 W of RF power.

The sample stage is mounted on the top of a 3D positioning stage manufactured by Attocube. The positioning stage's operation is based on the inertial slider principle (*9*). Three linear positioners give movement in x, y and z at 4 K by the use of piezoelectric elements, hence all actuation is done electrically.

3. Optical Interferometer Calibration

The cantilever interferometer must be calibrated to convert its voltage output to the cantilever's displacement. It is possible to do this by using our knowledge of the value of the wavelength of the light used by the interferometer. If the interferometer behaved ideally, the interference pattern, as represented by the voltage output of the interferometer, would have a purely sinusoidal dependence on the fiber-cantilever separation. However, due to imperfections in the interferometer not all the light impinging on the detector is part of the two interfering beams and results in a background signal that gives a DC offset to the output voltage,

$$V_o = V_{DC} + V_{AC} sin(4\pi(L + \delta L)/\lambda),$$

where L is the equilibrium separation between the end of the fiber and the cantilever and δL is the displacement of the cantilever. The sinusoidal dependence of V_0 on L and δL, and the value of wavelength of light are used to calibrate the interferometer.

Figure 2 illustrates the details of the signal sizes that the interferometer produces. The figure shows interferometer output, V_o versus cantilever displacement, δL. Also shown is the extra path length P the light must travel when the cantilever experiences a displacement δL, and the extra phase ϕ this represents in the argument of the sine in the V_o equation. Typically L is the order of

100 microns and δL is a few hundred nanometers peak-to-peak. The calibration begins by not oscillating the cantilever, δL = 0, and adjusting the wavelength of the light source, a semiconductor laser operating at ~1300 nm, so that $(4\pi L/\lambda) = n\pi$ hence, $sin(4\pi L/\lambda) = 0$. This means the cantilever is resting at δL = 0 and the AC component of V_0 is zero. This locates the cantilever at pt. 1 in figure 2. As the cantilever is displaced along +δL, V_o increases until at $\delta L = \lambda/8$, (pt. 2) where $V_o = V_{AC}$. At pt. 2 the two beams of light are interfering constructively to a maximum extent, i.e., they are perfectly in phase with each other. At this point the light must transverse the cantilever displacement twice, hence, $P = \lambda/4$. (Depending upon the sign of amplification in the electronics, they may instead be in perfect deconstructive interference. For the purposes of discussion, and without loss of generality, we assume they are in phase with each other.) The optical path length difference of one quarter of one wavelength corresponds to and extra π/2 phase. If the cantilever is displaced to $\delta L = -\lambda/8$, (pt. 3) then $V_o = -V_{AC}$. At pt. 3 the two beams of light are interfering destructively to a maximum extent, i.e., they are π out of phase with each other. If the cantilever is oscillated between $\delta L = \pm\lambda/8$ (between pts. 2 and 3) the cantilever moves a total distance $\delta L = \lambda/4$ peak-to-peak and the light travels a total distance $P = \lambda/2$ which corresponds to an extra phase of π.

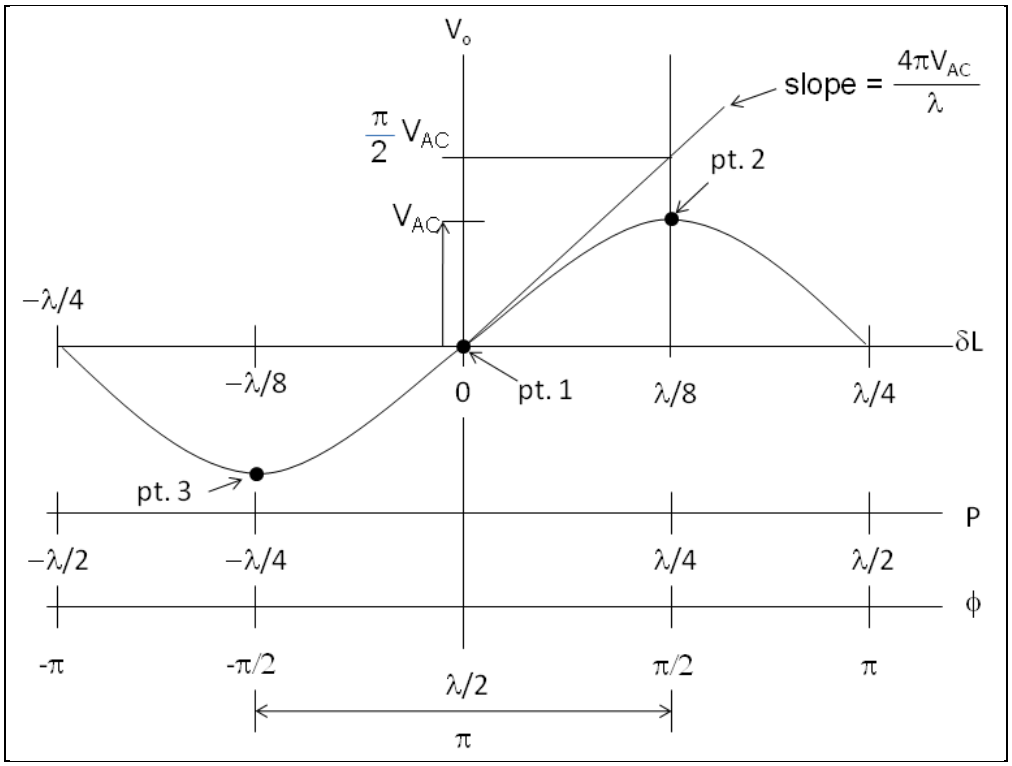

Figure. 2. Interferometer voltage output as a function of optical fiber-cantilever separation δL, optical path length P, and optical path length phase change ϕ. See text for detailed discussion.

Experimentally it is convenient to measure the RMS value of the cantilever oscillation. The information shown in figure 2 is re-plotted as RMS values in figure 3. The cantilever is at equilibrium at pt. 1 and at pt. 2, with a peak-to-peak displacement of $\lambda/4$, V_o has an RMS

amplitude of $V_{AC}/\sqrt{2}$. This amplitude is less than what it would be $2\sqrt{2}\pi V_{AC}/\lambda$ if the interferometer output did not roll over.

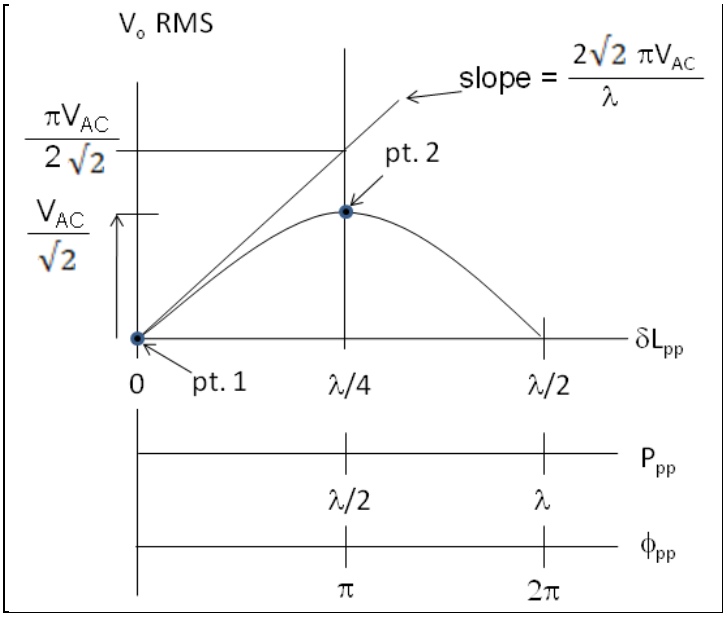

Figure 3. The RMS value of the AC component of the interferometer output as a function of the peak-to-peak value of the optical fiber-cantilever separation δL_{PP}, peak-to-peak value of the optical path length P_{PP}, and peak-to-peak value of the total optical phase change ϕ_{PP}. See text for a detailed discussion.

To determine the interferometer sensitivity, $V_o/\delta L$ as a function of cantilever oscillation amplitude the following procedure is used. The laser wavelength is adjusted so that $(4\pi L/\lambda) = n\pi$ hence $sin(4\pi L/\lambda) = 0$ locating the cantilever at pt. 1. The cantilever is then driven through a series of increasing amplitudes starting at δL ~25 nm to over 325 nm peak-to-peak, see the red points in figure 4. When the peak-to-peak displacement of δL is $\lambda/4$ the amplitude of the sine wave $V_{AC}sin(4\pi(L+\delta L)/\lambda)$ will be at a maximum, $2V_{AC}$ peak-to-peak. This point occurs at an SMU Drive Amp (V) of 2.0 V in figure 4. The SMU Drive Amp is a voltage that determines the amplitude of drive voltage used to base drive the cantilever. Using the knowledge of the cantilever displacement at pt. 2 allows us to calibrate the rest of the curve for cantilever displacement. We assume that a sine wave fits the raw data. The green curve in figure 4 is the sine wave fit to the location and amplitude at the curves peak. Given the quality of the sine wave fit to the data, we conclude that the conjecture that the data is sinusoidal was valid. Figure 4 displays the cantilever amplitude as an RMS value. The RMS value of the AC part of V_o at pt. 2 is $V_{AC}/\sqrt{2}$. Some measurements require a knowledge of the interferometer sensitivity near δL ~0. In this region a sine wave is well approximated as a straight line. In figure 4 this straight line is green. The slope of this line is $4\pi V_{AC}/\lambda$. At $\delta L = \pm\lambda/8$ the line has a peak-to-peak value of πV_{AC} and an RMS value of $V_{AC}/\sqrt{2}$. A cantilever displacement of $\delta L = \pm\lambda/8$ corresponds to 325 nm peak-to-peak or an RMS value of 114.9 nm.

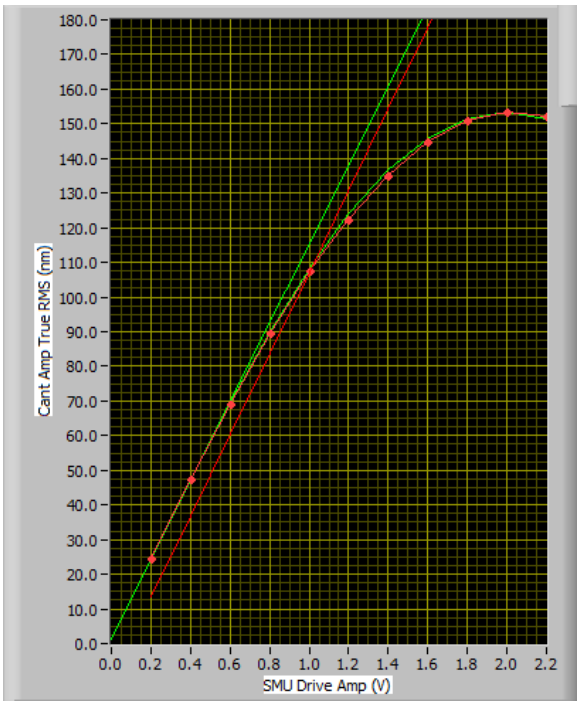

Figure 4. Fit of sine wave to raw data. Red dots are raw data, the red line connecting the red dots is an aid to the eye, the green curve is a sine wave fit to the data, the green straight line is a fit to the sine wave fit near zero. The red line should be ignored.

Once the calibration procedure has been accomplished, the output of the cantilever's displacement is converted from voltage to displacement. The next step in characterizing a cantilever is to experimentally determine its spring constant, k_c. The spring constant is related to the cantilever displacement through the equal partition theorem

$$k_c \langle x^2 \rangle = k_B T$$

where k_c is the cantilever spring constant, k_B is Boltzmann's constant, and T is the absolute temperature. The temperature can be measured with an independent temperature sensor, k_B is a known constant, and $<x^2>$ is the RMS value of the instantaneous position which we get from the converted cantilever displacement. A plot of $<x^2>$ versus T is made, resulting in a straight line with a zero intercept. The slope is the cantilever's spring constant. With the calibrated cantilever displacement and the cantilever's spring constant, we can now determine the temperature of the cantilever under both undriven and driven circumstances, referred to Brownian motion for the undriven case and Frequency Noise in the driven case. For the undriven case, the temperature of the cantilever can be found using the equal partition theorem stated above. The second technique for measuring Brownian motion involved measuring the frequency noise of a driven cantilever. A driven cantilever is excited to constant oscillation

amplitude at its natural resonance frequency. In this case the temperature can be found using the following relationship (*16*),

$$P_{\delta x}^{therm}(f) = \frac{k_B T}{2\pi^2 \chi_{rms}^2 k \tau_0}$$

where τ_0 is the time constant of the cantilever at each temperature measured. It is experimentally determined by letting the cantilever ring down.

4. Results and Discussion

Utilizing the CERMIT protocol, we measure the real time recovery of the polarization during an inversion-recovery experiment by monitoring the frequency of the driven cantilever. The signal, which is proportional to the magnetization along the Zeeman axis, is registered by recording changes in the resonance frequency of a driven cantilever. We use a digital frequency controller (*12*) to drive the cantilever at the resonant frequency of its lowest bending mode. The magnetic-field gradient from the Ni particle's magnetic moment interacts with the nuclear spins in the sample, causing the resonance frequency of the cantilever to shift slightly as the sample's magnetization is modified, i.e., as part of it, the Ga69, is inverted. The initial Ga69 polarization is inverted with a 20 ms long, wide ARP sweep through the entire region of spins contained in the bulk (*13*) and image slice regions, as shown in figure 5. The RF is only on during the 20 ms ARP, while the spins are being adiabatically inverted. After inverting the polarization, the frequency of the driven cantilever is monitored as the polarization realigns along the Zeeman axis. The spin-lattice relaxation time T_1, can then be directly extracted from the recovery curve using the time dependent magnetization relation for inversion recovery:

$$M_z/M_0 = 1 - 2 * e^{\left(-t/T_1\right)}$$

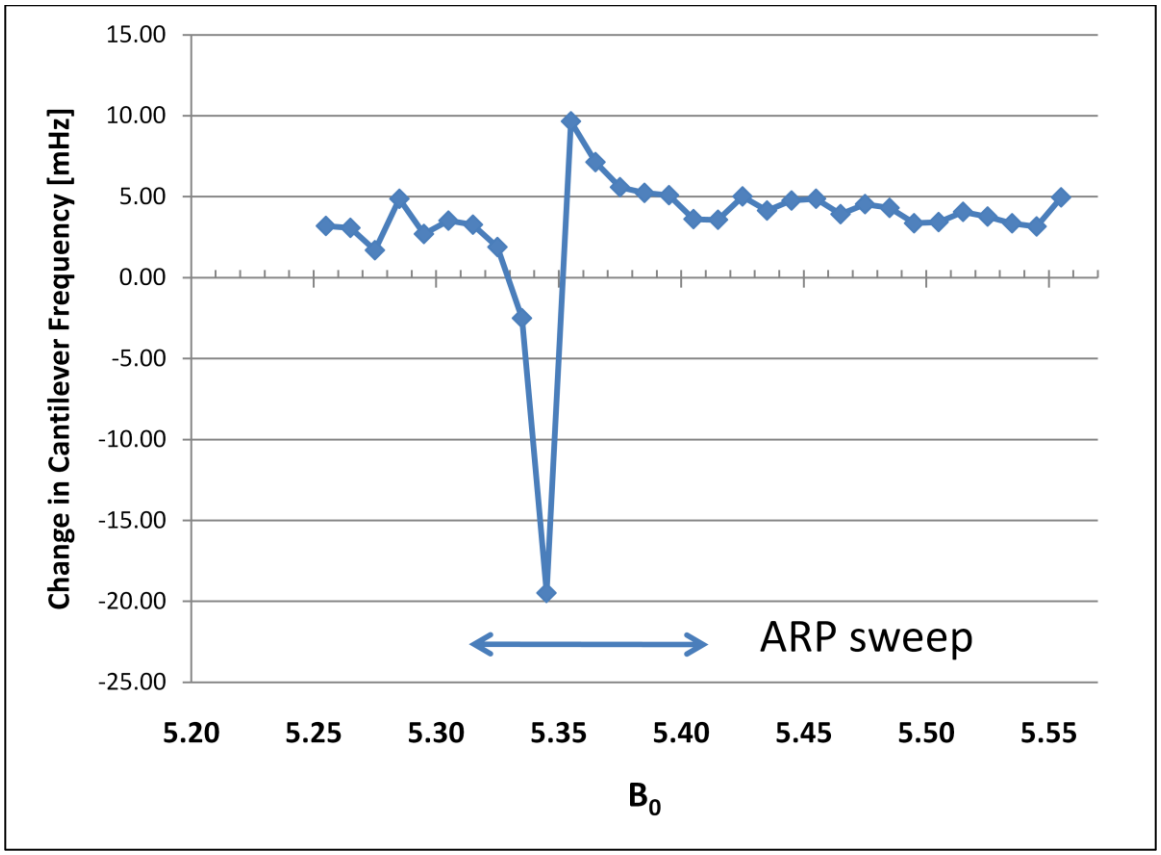

Figure 5. A typical MRFM scan utilizing the CERMIT protocol. Changes in the cantilever's frequency, which are proportional to the magnetization along the Zeeman axis, are shown as the background magnetic field B_0 is swept. A wide ARP sweep is done through the entire region of bulk and slice spins to invert the spins and measure T_1 during inversion recovery.

The temperature of the sample was adjusted from the probe's base temperature of 4.8 K to 9.3, 16.7 and 24.9 K by directly heating the sample stage holder. At each temperature change, the system was allowed to reach thermal equilibrium, as monitored by the probe's thermometer. Prior to recording the inversion recovery at each temperature, the sample was positioned at a distance of 300 nm from the magnetic particle on the cantilever. The distance is determined by an interferometer on the sample stage axis that measures the relative displacement of the sample distance from the cantilever tip. The amplitude of the driven cantilever was maintained constant by recalibrating the cantilever's amplitude vs. drive effort at each temperature, while maintaining a distance of 300 nm from the surface. Since our signal is registered as changes in the cantilever frequency and the cantilever frequency is highly dependent on the tip-sample distance, the tip-sample distance was set once the probe had reached thermal equilibrium. The sample stage interferometer was then used to monitor any displacement of the sample relative to the tip. The stage interferometer measured small changes in position over time while the probe head reached equilibrium. Two possible sources of this drift are small probe head dimensional changes due to thermal contraction or expansion and drift in the sample stage position, possibly due to creep in the piezoelectric element. Care was taken to record inversion recovery data only after the probe

head had achieved equilibrium. Figure 6 shows the effect of stage drift on cantilever frequency. Figure 6a shows the gradient in cantilever frequency overlaid with the frequency changes as the sample stage reaches equilibrium. Since the frequency changes observed here are small it is reasonable to assume that stage motion is causing the changes in the cantilever's frequency. Figure 6b is representative of the probe head at equilibrium, and a drift in cantilever frequency or stage position is not observed.

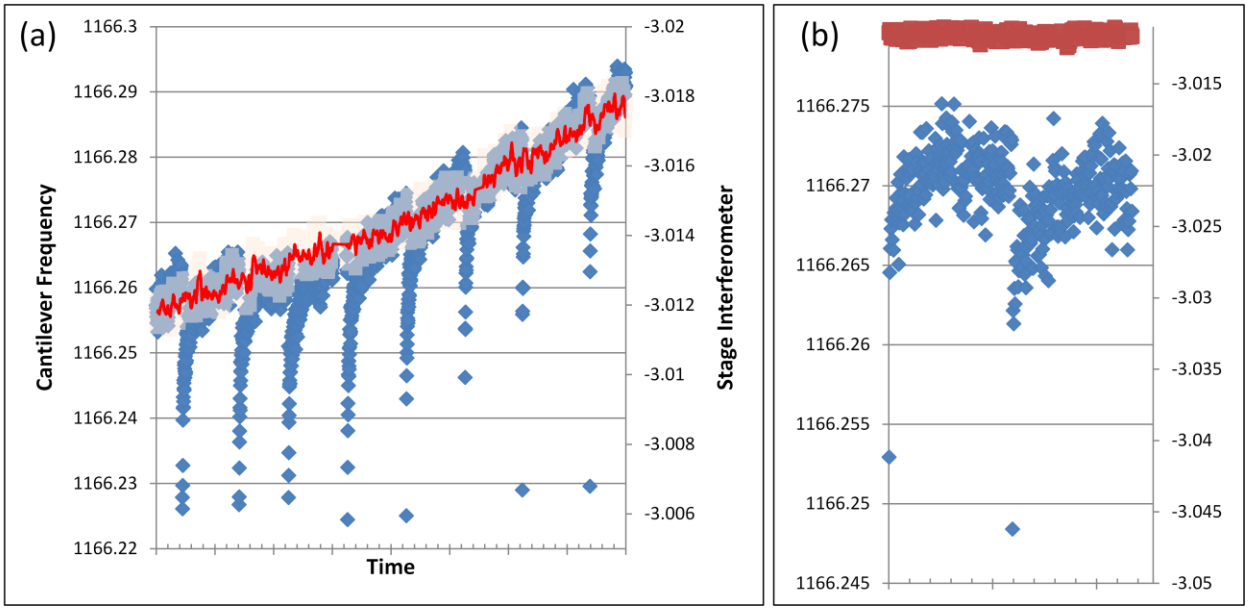

Figure 6. The stage interferometer (in red) is used to track the relative position of the sample to the cantilever tip while the cantilever frequency (in blue) is being recorded. ARPs are used to invert the spins for inversion recovery. (a) A typical example of the sample stage not yet in equilibrium. The tip-sample distance is changing, causing an overall gradient in the cantilever frequency. (b) Once the system is in equilibrium, T_1 can be measured by monitoring the cantilever's frequency.

Figure 7 shows typical inversion recovery data and results of the exponential fits at the four temperatures of 4.8, 9.3, 16.7, and 24.5 K which are summarized in table 1. Data was collected with a B_1 of 1.06 mT (requires 1 W of RF power). By keeping B_1 constant the same fraction of the initial nuclear polarization was inverted each time. This permits a direct comparison of the magnetization magnitudes in terms of cantilever frequency changes. Data was collected with a tip-sample separation of 300 nm, with the exception of the T = 24.9 K data. It was necessary to increase the tip-sample separation for this case because the magnitude of the noise in the cantilever frequency caused by surface noise (*14*) was significant enough to obscure the measurement. Effects due to surface noise have previously been shown to increase with sample temperature. Since the frequency changes became so small at 24.9 K, we also found it necessary to increase B_1 from 1.06 mT to 1.7 mT to increase the polarization fraction being inverted. Figures 7a, b, and c show data collected at B_1 = 1.06 mT. Figure 7d shows data collected at both B_1 = 1.06 and 1.7 mT. The data displaced to the right by 100 s was collected at 1.06 mT, the data beginning at 0 s was collected at 1.7 mT. Figure 8 shows the temperature dependence of T_1 and

the net magnetization in terms of the measured cantilever frequency. The net magnetization behaves linearly with the inverse of the temperature as is predicted by theory (*15*). Figure 8b shows the relaxation rate $1/T_1$ with temperature. As can be seen in figure 8b, a transition temperature occurs near T ~ 20K. This has been previously observed using traditional NMR (*2*). The recovery laws which effect the relaxation rate, can be dominate in different temperature regimes. The total spin-lattice relaxation rate has contributions from magnetic relaxation which is weakly temperature dependent and, for GaAs, there is time-dependent quadrupolar relaxation interaction mechanism which is strongly temperature dependent. As with traditional NMR, MRFM can be used to examine the different relaxation rate mechanisms and their temperature dependence. The two advantages of MRFM are that T_1 can be measured in real time and picogram quantities of material can be studied.

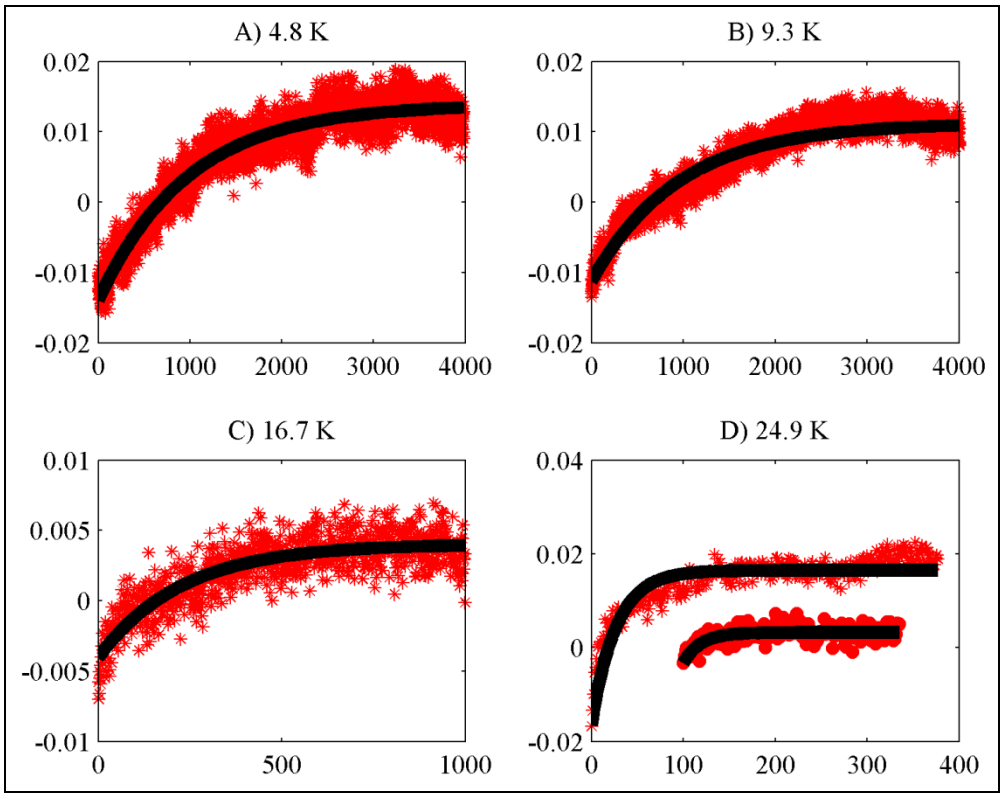

Figure 7 (a–d). Typical inversion recovery data for the recorded temperatures: 4.8; 9.3; 16.6; 24.9 K. At t = 0 s the ARP is applied using the RF coil which generates the B_1, inverting the spins in the sample and causing a change in the cantilever's natural frequency. During spin inversion recovery, the cantilever tracks back to the initial condition of spins aligned with B_0. The curves are fit with the standard inversion recovery exponential form.

Table 1. Measured T_1 and net magnetization values as a function of temperature from fitted data shown in figure 7.

Temperature [K]	T_1 (s)	Magnetization [mHz]
4.8	1340.224	0.0300335
9.3	876.458	0.0247917
16.7	184.114	0.0102456
24.9	25.39	0.00713975

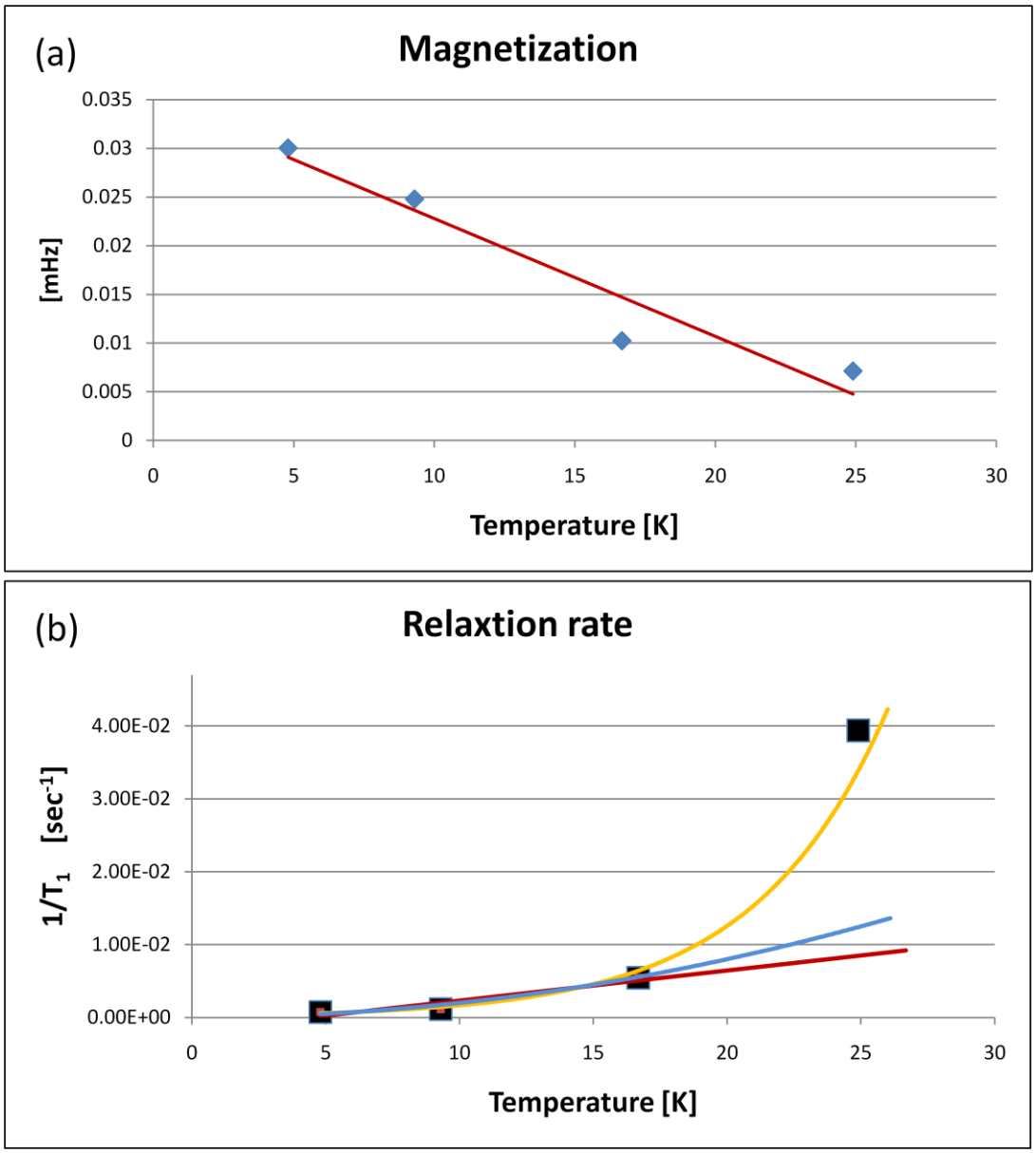

Figure 8 (a–b). Magnetization and Relaxation rate as a function of temperature. (a) Magnetization is linear with the inverse of temperature as predicted by theory (*15*). (b) The relaxation rate $1/T_1$. T^{-1} (red), T^{-2} (blue) and $\exp(1/T_1)$ (yellow) curves are shown along with the data. The total relaxation rate can depend on several mechanisms which become dominant in different temperature regimes (*2*).

5. Conclusions

The technique demonstrated here significantly reduces the experimental time required for a spin-lattice inversion recovery measurement. Real time monitoring of the spin-lattice relaxation time T_1 as a function of sample temperature has been demonstrated with MRFM using a force gradient detection protocol. The temperature dependence is in line with previous studies done on GaAs (2). Changes in the net magnetization stored along the Zeeman axis is registered as a change in the driven cantilever's resonant frequency. By tracking the cantilever's resonant frequency, after an inversion in the sample's magnetization, an entire inversion recovery curve can be obtained in a time the order of T_1. Using traditional NMR T_1 measurement techniques capturing the entire inversion recovery curve in N points would require N measurements spaced $\sim T_1$ apart for a total time the order of $N*T_1$.

6. References

1. Takigawa, M.; Reyes, A. P.; Hammel, P. C.; Thompson, J. D.; Heffner, R. H.; Fisk, Z.; Ott,K. C. Cu and O NMR Studies of the Magnetic Properties of YBa2Cu3O6.63 (Tc=62 K). *Phys Rev B 43* **1991**, , 247–257.
2. McNeil, J. A.; Clark, W. G. Nuclear Quadrupolar Spin-lattice Relaxation in Some III-V Compounds. *Phys. Rev. B 13* **1976**, 4705.
3. Schoeniger, J. S.; Aikenm N.; Hsu, E.; Blackband, S,J. Relaxation-time and Diffusion NMR microscopy of single neurons. *J Magn Reson B.* **1994 Mar**, *103* (3), 261–73.
4. Private communication, John Marohn, 2005
5. Sidles, J. A., et al. Magnetic Resonance Force Microscopy. *Rev. Mod. Phys.* **1 Jan. 1995**, *67* (1), 249.
6. Marohn, J. A.; Fainchtein, R.; Smith, D. D. An Optimal Magnetic Tip Configuration for Magnetic-resonance Force Microscopy of Microscale Buried Features. *Appl. Phys. Lett.* **21 Dec. 1998**, *74* (25), 3778.
7. Garner, S. R., et al. Force-gradient Detected Nuclear Magnetic Resonance. *Appl. Phys. Lett.* **21 June 2004**, *84* (25), 5091.
8. Private communication, Raul Fainchtein, 1996
9. Pohl, D. W. Sawtooth Nanometer Slider: A Versatile Low Voltage Piezoelectric Translation Device. *Surface Sci.* **1 March 1987**, *181* (102), 174.
10. Doran Smith, unpublished results
11. Swartz, E. T. Efficient He-4 Cryostats for Storage Dewars. *Rev. Sci. Instrum.* **1986**, *57* (11), p. 2848.
12. SC-Solutions Frequency Controller, model number scFDC.
13. Suter, A., et al. Probe-Sample Coupling in the Magnetic Resonance Force Microscopy. *J Magn. Res.* **2002**, *154*, 210.
14. Yazdanian, S. M.; Marohn, J. A.; Loring, R. F. Dielectric Fluctuations in Force Microscopy: Noncontact Friction and Frequency Jitter. *J. Chem. Phys.* **2008**, *128*, 224706.
15. Abragam, A. The Principles of Nuclear Magnetism, p. 2, equ. 2, 1961.
16. Marohn, J. Frequency Noise, white paper, Cornell University, 24 February 2008.

List of Symbols, Abbreviations, and Acronyms

ARP	adiabatic rapid passage
CERMIT	cantilever enhanced resonance magnetization inversion transients
FID	free induction decay
MRFM	magnetic resonance force microscopy
SPAM	springiness preservation by aligning magnetization

NO. OF COPIES	ORGANIZATION
1 ELEC	ADMNSTR DEFNS TECHL INFO CTR ATTN DTIC OCP 8725 JOHN J KINGMAN RD STE 0944 FT BELVOIR VA 22060-6218
1 CD	OFC OF THE SECY OF DEFNS ATTN ODDRE (R&AT) THE PENTAGON WASHINGTON DC 20301-3080
1	US ARMY RSRCH DEV AND ENGRG CMND ARMAMENT RSRCH DEV & ENGRG CTR ARMAMENT ENGRG & TECHNLGY CTR ATTN AMSRD AAR AEF T J MATTS BLDG 305 ABERDEEN PROVING GROUND MD 21005-5001
1	US ARMY INFO SYS ENGRG CMND ATTN AMSEL IE TD A RIVERA FT HUACHUCA AZ 85613-5300
1	COMMANDER US ARMY RDECOM ATTN AMSRD AMR W C MCCORKLE 5400 FOWLER RD REDSTONE ARSENAL AL 35898-5000
1	US GOVERNMENT PRINT OFF DEPOSITORY RECEIVING SECTION ATTN MAIL STOP IDAD J TATE 732 NORTH CAPITOL ST NW WASHINGTON DC 20402
14	US ARMY RSRCH LAB ATTN IMNE ALC HRR MAIL & RECORDS MGMT ATTN RDRL CIO LL TECHL LIB ATTN RDRL CIO MT TECHL PUB ATTN RDRL SEE O D A ALEXSON (10 HCS) ATTN RDRL SEE O D D SMITH ADELPHI MD 20783-1197